*applied sciences*

MDPI

*Article*

# Nonlinear Analysis and Solution for an Overhead Line Magnetic Energy Harvester with an Active Rectifier

**Alexander Abramovitz *, Moshe Shvartsas and Alon Kuperman ***

School of Electrical and Computer Engineering, Ben-Gurion University of the Negev, P.O. Box 653, Beer-Sheva 84105, Israel; meishe@bgu.ac.il

* Correspondence: alexabr@tauex.tau.ac.il (A.A.); alonk@bgu.ac.il (A.K.)

**Abstract:** Recently, there has been a significant focus on developing various energy harvesting technologies to power remote electronic sensors, data loggers, and communication devices for smart grid systems. Among these technologies, magnetic energy harvesting stands out as one straightforward method to extract substantial power from current-carrying overhead lines. Due to the relatively small size of the harvester, the high currents in the distribution system quickly saturate its magnetic core. Consequently, the magnetic harvester operates in a highly nonlinear manner. The nonlinear nature of the downstream AC to DC converters further complicates the process, making precise analytical modeling a challenging task. In this paper, a clamped type overhead line magnetic energy harvester with a controlled active rectifier generating significant DC output power is investigated. A piecewise nonlinear analytical model of the magnetic harvester is derived and reported. The modeling approach is based on the application of the Froelich equation. The chosen approximation method allowed for a complete piecewise nonlinear analytical treatise of the harvester's behavior. The main findings of this study include a closed-form solution that accounts for both the core and rectifiers' nonlinearities and provides an accurate quantitative prediction of the harvester's key parameters such as the transfer window width, optimal pulse location, average DC output current, and average output power. To facilitate the study, a nonlinear model of the core was developed in simulation software, based on parameters extracted from core experimental data. Furthermore, theoretical predictions were verified through comparison with a computer simulation and experimental results of a laboratory prototype harvester. Good agreement between the theoretical, simulation, and experimental results was found.

**Keywords:** magnetic cores; analytical models; saturation magnetization; magnetic flux; magnetic energy harvesting

check for updates

**Citation:** Abramovitz, A.; Shvartsas, M.; Kuperman, A. Nonlinear Analysis and Solution for an Overhead Line Magnetic Energy Harvester with an Active Rectifier. *Appl. Sci.* **2024**, *14*, 11178. https://doi.org/10.3390/app142311178

Academic Editors: Alessandro Lo Schiavo and Roberto Zivieri

Received: 15 October 2024
Revised: 15 November 2024
Accepted: 27 November 2024
Published: 29 November 2024

**Copyright:** © 2024 by the authors. Licensee MDPI, Basel, Switzerland. This article is an open access article distributed under the terms and conditions of the Creative Commons Attribution (CC BY) license (https://creativecommons.org/licenses/by/4.0/).

## 1. Introduction

Electrical power transmission systems are, perhaps, the world's largest technical installations. Transmission lines span over vast distances, often pass through remote and hardly accessible locations, and are prone to the forces of nature. To alleviate the task of inspection of power systems, monitoring equipment based on smart sensors [1–3], remote cameras [4,5], etc., have recently been developed. To power such electronic devices, several types of magnetic energy harvesters have been proposed [6]. Compared to other energy harvesting methods, a magnetic energy harvester is a mechanically rugged device that has the advantage of higher reliability and greater power density.

An overhead line magnetic energy harvester (OLMEH) is designed to clamp onto a transmission line and convert the magnetic energy generated by the line current into DC power. The OLMEH aims to power electronic equipment or, in most cases, charge a battery. The concept of an OLMEH is similar to that of a current transformer (CT) [7]. Yet, the operational conditions of a CT and an OLMEH are quite different. The CT is operated under a short circuit (or very low impedance) load to keep the core within the linear region,

whereas the OLMEH operates with a constant voltage load. To exploit the full range of B-H characteristics, OLMEH's core is usually allowed to run into the saturation regions. The inherent nonlinearity of the magnetic core makes the OLMEH's analysis and design a challenging problem [6–9]. Furthermore, extracting the full available power that the OLMEH can provide requires properly matching the OLMEH parameters to attain the maximum power point conditions [10].

An additional advantage of an OLMEH is that it can harvest the energy from a multi-kV level AC transmission line to power electronic devices operating at a low DC voltage of only a few volts [11–14] while avoiding the application of bulky high-voltage step-down transformers, thus saving hardware and installation costs.

To derive the DC voltage, an OLMEH requires a suitable power electronics interface, which can be either passive or active. Passive OLMEHs utilize uncontrolled diode bridge rectifiers to implement the AC-DC conversion, offering simplicity and higher reliability [10,15]. To maximize the power density, the OLMEH should be matched to the load (typically of a constant voltage type) by appropriate selection of cross-sectional area of the core and number of secondary winding turns. Therefore, such an approach is referred to as "maximum power point matching" (MPPM) and allows for maximizing the harvested OLMEH power for a wide range of primary current magnitudes [16]. Yet, in cases where the CVL is a battery, its voltage is expected to vary depending on its charging state. Thus, only near-optimal matching can be attained.

Active rectification is another viable approach to attain DC power at OLMEH's output. One possible configuration of an OLMEH-based charger with an active rectifier operating under a constant voltage load (CVL) is illustrated in Figure 1. The idea behind this circuit is to short-circuit the OLMEH's secondary winding so to preserve the stored magnetic energy and then release it towards the load under optimal conditions. This helps to increase the power output of the circuit, allows control over the depth of saturation, and, enables the implementation of overcharge and overcurrent protection features. Moreover, the active rectifier allows the application of better maximum power point tracking (MPPT) [17–19], which can help attain a higher power under variable line current conditions.

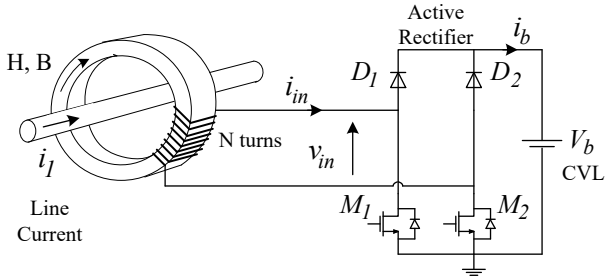



**Figure 1.** Overhead line magnetic energy harvester with an active rectifier feeding a constant voltage load.

The circuit in Figure 1 was investigated in the recent literature [19–22], which suggests several approaches to deal with the challenging problem of core nonlinearity. For instance, its earlier counterpart [19] applied a cot(*) function to accurately model core nonlinearity. Yet, due to the complex nature of such an approximating function, after a few theoretical steps, the final solutions were obtained only numerically.

This article aims to develop an approximated, yet complete, nonlinear analytical model and solution for an overhead line magnetic energy harvester with an active rectifier (OLMEH-AR), under a constant voltage load, as shown in Figure 1.

The proposed model is derived by applying piecewise nonlinear analysis, relying on the Froelich equation to model the B-H characteristics of the magnetic core. The Froelich approximation is based on a first-order rational function. The advantage of the offered approach is that it lends itself to the analytical treatise. The result is a complete closed-form

analytical solution to the problem that is quite accurate, simple, and suited for engineering applications.

The rest of the paper is as follows: simulated waveforms, state analysis, and derivation of equivalent circuits are given in Section 2; also, this section presents the analytical model of the OLMEH-AR and derives the expressions for the power transfer window, output current, and the output power and the conditions for maximum power. Experimental measurements of a laboratory prototype are reported in Section 3 and stand in good agreement with the proposed theoretical predictions.

## 2. The Applied Methodology

### *2.1. State Analysis and Equivalent Circuits*

Analysis of the OLMEH-AR started with computer simulation (PSIM v. 9.1). Derivation of the computer model of the magnetic core in PSIM v9.1 software is a tedious trial-and-error process; however, the computer simulation model proved to be an indispensable tool in the undertaken study.

Examination of the simulated waveforms of the OLMEH-AR in Figure 2 reveals that its operation period comprises two symmetrical half cycles. The positive half-cycle commences when the secondary current becomes positive, $i_2(t) > 0$ and comprises four states. Note that during the negative half-cycle, a similar order of events occurs (with $M_2$ interchanging its function with $M_1$ and $D_2$ interchanging its function with $D_1$). Therefore, it is sufficient to analyze only the positive half-cycle.

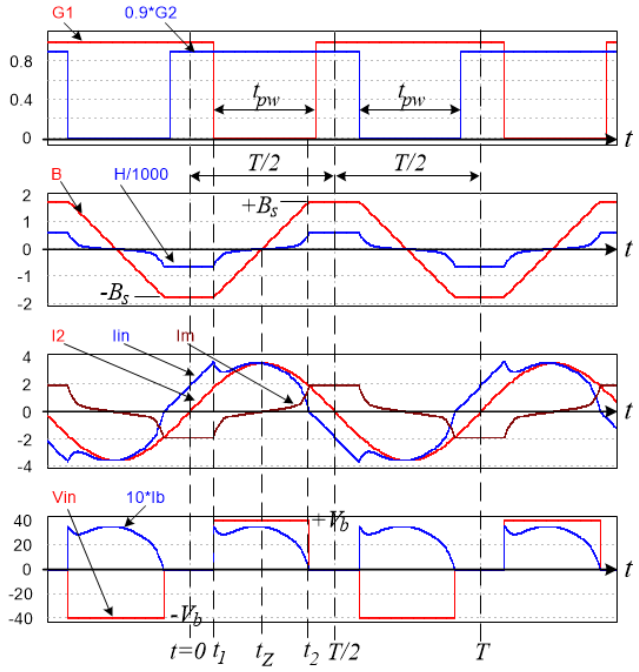



**Figure 2.** Typical simulated waveforms of an OLMEH-AR under CVL.

State 1 [0, $t_1$], see Figure 3a, commences at $t = 0$. Here, both active switches conduct and effectively short the secondary winding.

State 2 [$t_1$, $t_2$], see Figure 3b, commences at $t = t_1$, when, by the controller's command, the $M_1$ switch is turned off but $M_2$ remains on. Here, the rectifier diode $D_1$ turns on and allows the current to charge the battery. Since a constant battery voltage is applied to the secondary winding, the flux density in the core starts ramping up linearly, while causing the magnetizing current to rise in a nonlinear fashion.

State 3 [$t_2$, $t_1 + t_{pw}$], see Figure 3c, commences at $t = t_2$ when the rectifier currents drop to zero, $i_{in} = i_b = 0$. Here, the anti-parallel diode of the $M_1$ switch starts conducting and shorts the secondary winding.

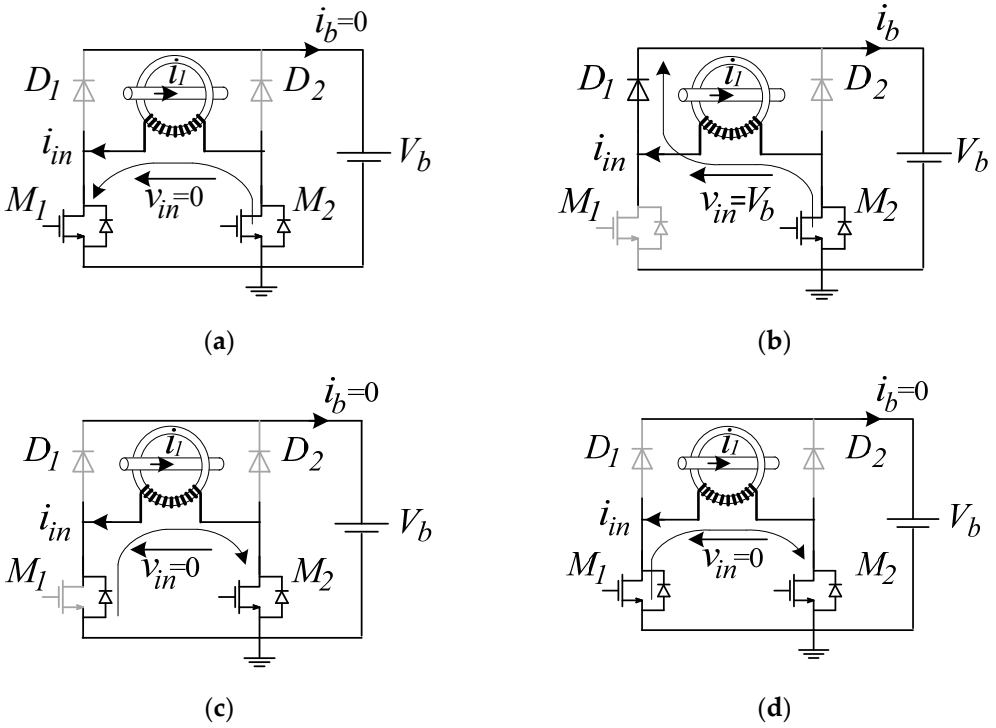



**Figure 3.** Semiconductor conduction states during State 1 (**a**); State 2 (**b**); State 3 (**c**); and State 4 (**d**).

State 4 [$t_1 + t_{pw}$, $T/2$], see Figure 3d, commences when, by the controller's command, switch $M_1$ is turned on again and helps its anti-parallel diode to keep the winding shorted. Under short circuit conditions, the flux density in the core remains constant until the end of the positive half cycle.

The OLMEH-AR model based on a simplified cantilever model with a saturable magnetizing inductance, $L_m$, placed on the secondary winding, while neglecting the leakage inductance, is shown in Figure 4a. The ideal transformer $1 : N$ acknowledges the fact that the line conductor acts as a single-turn primary winding, while the secondary one consists of the $N$ turn wound on the OLMEH's core. The simplified equivalent circuit of the short-circuit (SC) state (States 1, 3, and 4) is shown in Figure 4b, and the simplified model of State 2, the only charging state (CS) that allows current to the load, is presented in Figure 4c.

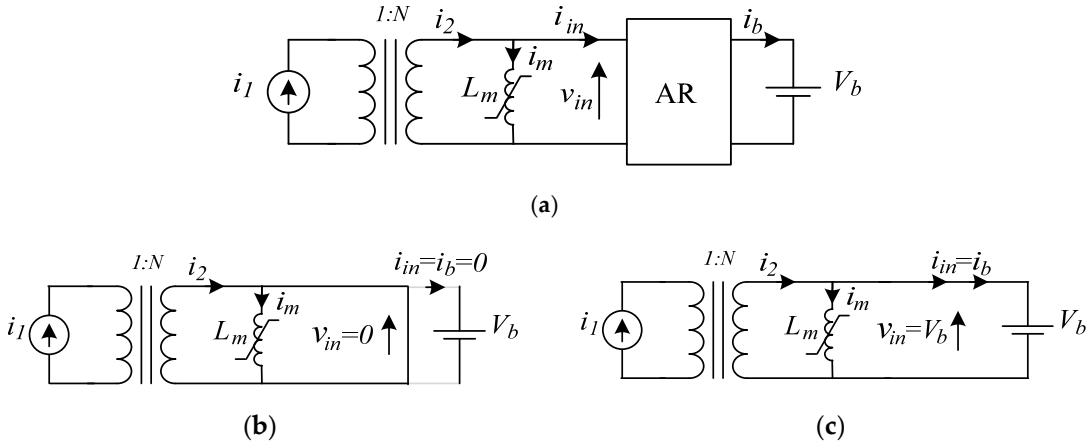



**Figure 4.** General model of the overhead line magnetic energy harvester with an active rectifier (OLMEH-AR) with a constant voltage load (**a**); its equivalent short circuit States 1, 3, and 4 (**b**) and the equivalent charging State 2 (**c**).

### *2.2. The Froelich Equation Review*

To facilitate the analysis approach, the following simplifying assumptions are adopted.

Firstly, ideal (lossless) rectifiers and ideal switches are assumed with no voltage drop and zero ON resistance. Secondly, the core is assumed to be un-hysteretic (lossless), whose nonlinearity can be described by the Froelich equation:

$$B(H) = \frac{aH}{b+H}, \tag{1}$$

Here, the parameter $a$ is the saturation flux density at infinite field intensity:

$$B_{sat} = \lim_{H\to\infty} \frac{aH}{b+H} = a, \tag{2}$$

whereas $b$ is related to the magnetic permeability of the core at the low field intensity (linear) region

$$\mu(H \ll b) = \frac{a}{b} \tag{3}$$

*2.3. Analysis: Power Transfer Window*

The following definitions are introduced: $N$ is the number of OLMEH secondary turns, $I_{1m}$ is the line (primary) current amplitude, and $I_{2m} = I_{1m}/N$ is the amplitude of the secondary current. As usual, $f = 1/T = \omega/2\pi$ is the line frequency.

Examining the waveforms in Figure 2 reveals that the magnetic flux density swings from its initial negative saturation value $B(t_1) = -B_s$ towards the positive saturation value $B(t_2) = +B_s$. The transition is linear since it results from the application of the constant voltage $V_b$ to the secondary winding; see Figures 3b and 4c. Therefore

$$B(t_2) = +B_s = \frac{1}{NA_c}\int_{t_1}^{t_2} V_b dt - B_s, \tag{4}$$

whence

$$B_s = \frac{V_b}{2NA_c}(t_2 - t_1), \tag{5}$$

The practical saturation level that the core can reach, $B_s$, is presumed to be lower than the heavy saturation flux density level, $B_s < B_{sat}$, defined by (2).

The time interval that appears in (5)

$$T_w = (t_2 - t_1), \tag{6}$$

is defined as the power transfer window. To allow the charging current pulse to terminate naturally, the pulse width, $t_{pw}$, set by the controller, see Figure 2, has to be appropriately matched so that $t_{pw} > T_w$. Switching the MOSFET on, see Figure 3d, decreases the resistance of the conductive path, minimizes the conduction losses during the SC states, and so increases the OLMEH's conversion efficiency.

Combining (5) with the Froelich Equation (1) yields the magnetic field intensity attained by the core at the peak of saturation:

$$H(t_2) = H(B_s) = \frac{bB_s}{a - B_s} = \frac{b\frac{V_b}{2NA_c}(t_2 - t_1)}{a - \frac{V_b}{2NA_c}(t_2 - t_1)} = \frac{N}{l_c} i_m(t_2), \tag{7}$$

The right-hand side of (7) was attained by Ampere's law.

Further examination of the waveforms in Figure 2 suggests that charging State 2 is terminated when the magnetizing current equals the secondary current:

$$i_m(t_2) = i_2(t_2) = I_{2m}\sin(\omega t_2), \tag{8}$$

Hence, substituting (8) into (7) yields

$$\frac{b\frac{V_b}{2NA_c}(t_2 - t_1)}{a - \frac{V_b}{2NA_c}(t_2 - t_1)} = \frac{N}{l_c} I_{2m} \sin(\omega t_2), \tag{9}$$

Since $t_1$ is set by the controller and assumed to be known, (9) is an equation of a single variable $t_2$. Yet, (9) is difficult to solve. A straightforward approach to obtain the solution of (9) is to proceed with numerical analysis. An alternative approach offered here is obtaining an analytical solution through approximation of the sine function on the right-hand side of (9) by a rational function, considering that the range of interest lies somewhere in $\frac{2}{3}\pi < \omega t < \frac{5}{6}\pi$. As a compromise between complexity and accuracy, it is suggested to approximate the falling segment of the sine function using

$$\sin(\omega t) \approx \frac{K_1(\pi - \omega t)}{K_2 - \omega t}, \tag{10}$$

With $K_1 = 3.232$ and $K_2 = 6.003$, (10) agrees with the $\sin(\omega t)$ function at 120°, 150°, and 180°, thus providing good accuracy within the range of interest. A comparison plot of the $\sin(\omega t)$ function to the chosen approximation function (10) is shown in Figure 5.

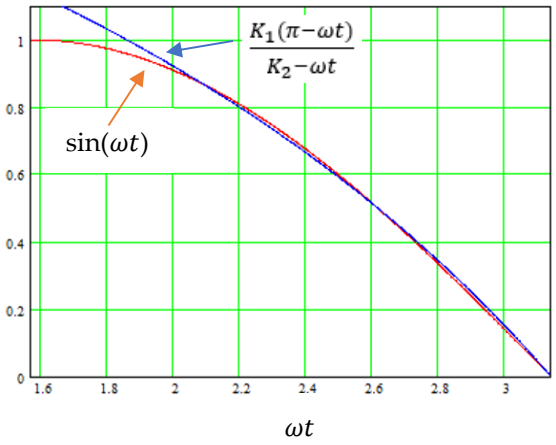



**Figure 5.** Comparison plot of the $\sin(\omega t)$ function to the chosen approximation function (10) (for $K_1$ = 3.232 and $K_2$ = 6.003).

Substitution of (10) into (9) yields

$$\frac{l_c}{N} \frac{b\left[\frac{V_b}{NA_c}(t_2 - t_Z)\right]}{a - \left[\frac{V_b}{NA_c}(t_2 - t_Z)\right]} = I_{2m} \frac{K_1(\pi - \omega t_2)}{K_2 - \omega t_2}, \tag{11}$$

Introducing the definitions of the normalized time

$$t_N = \frac{\omega}{\pi} t, \tag{12}$$

the normalized secondary current

$$I_N = \frac{I_{2m}}{I_{base}} = \frac{N I_{2m}}{b l_c} = \frac{I_{1m}}{b l_c}, \tag{13}$$

the normalized load voltage

$$V_N = \frac{V_b}{V_{base}} = \frac{\pi V_b}{\omega a N A_c}, \tag{14}$$

and applying (12)–(14) to (11) yields the normalized equation:

$$\frac{V_N(t_{2N}-t_{1N})/2}{1-V_N(t_{2N}-t_{1N})/2}=I_N\frac{K_1\pi(1-t_{2N})}{K_2-\pi t_{2N}}, \tag{15}$$

which, after some manipulation, can be written in the form of a standard quadratic equation:

$$\alpha t_{2N}^2+\beta t_{2N}+\gamma=0, \tag{16}$$

where the coefficients are

$$\alpha=\frac{\pi}{2}V_N(1+K_1I_N), \tag{17}$$

$$\beta=-\left[\pi K_1I_N+\frac{\pi}{2}K_1(1+t_{1N})V_NI_N+\frac{1}{2}(\pi t_{1N}+K_2)V_N\right], \tag{18}$$

$$\gamma=\pi K_1I_N+\frac{\pi}{2}K_1t_{1N}V_NI_N+\frac{K_2}{2}t_{1N}V_N, \tag{19}$$

Only the solution for $t_{2N}<1$ (i.e., $t_2<T/2$) has a physical meaning, therefore:

$$t_{2N}=\frac{-\beta-\sqrt{\beta^2-4\alpha\gamma}}{2\alpha}, \tag{20}$$

Translating (20) from the normalized time to the real-time, see (12), gives the termination instant of charging State 2:

$$t_2=\frac{T}{2}t_{2N}, \tag{21}$$

Since the firing instant $t_1$ is set by the controller and is known and the extinction instant $t_2$ can be obtained from (21), the power transfer window can be found by (6). This allows for the calculation of the output power of the OLMEH-AR as shown next.

### *2.4. Analysis: Output Current and Power*

The rectifier's input current is the difference between the secondary current, $i_2(t)$, and the magnetizing current, $i_m(t)$; see Figure 4c. Therefore, the charge delivered to the CVL during a half cycle is

$$q_b=\int_{t_1}^{t_2}(i_2(t)-i_m(t))dt, \tag{22}$$

Examining the waveforms in Figure 2 reveals that in the steady-state, the magnetizing current is symmetrical. This means that the charge drawn by the magnetizing current is zero:

$$\int_{t_1}^{t_2}i_m(t)dt=0, \tag{23}$$

This also complies with the principle that for the lossless system in the steady state, the energy captured by an ideal magnetizing inductance is fully recycled.

Combining (22) and (23), the average output current can be found as:

$$I_b=\frac{2}{T}\int_{t_1}^{t_2}I_{2m}\sin(\omega t)dt=\frac{I_{2m}}{\pi}(\cos(\omega t_1)-\cos(\omega t_2)), \tag{24}$$

whence the average output power delivered to the constant voltage load is

$$P_o=V_bI_b=\frac{2\sqrt{2}}{\pi N}V_bI_{1rms}(\cos(\omega t_1)-\cos(\omega t_2)), \tag{25}$$

### *2.5. Analysis: Maximum Power Conditions*

Recall again that the delay time, $t_1$, in (25) is an independent variable set by the controller's command, whereas $t_2$, given by (20), (21) is a function of $t_1$ as well as the

OLMEH's parameters and operation conditions. Thus, the question arises regarding the proper choice of the delay time to optimize/maximize the OLMEH's power output. Symmetry considerations, see Appendix A for details, suggest that the maximum output power can be attained when the power transfer window is aligned symmetrically to the line current peak:

$$t_{2_{mpp}} = \frac{T}{2} - t_{1_{mpp}}, \tag{26}$$

Substituting (26) into (25), the maximum power that can be obtained from the OLMEH-AR under the MPP condition is

$$P_{ompp} = \frac{4\sqrt{2}}{\pi N} V_b I_{1rms} \cos(\omega t_{1mpp}), \tag{27}$$

Whereas the optimum delay time, $t_{1_{mpp}}$, required to implement the MPP condition is found by normalizing the condition (26) and substituting it into (15). Further manipulation of the expression leads to the following quadratic equation:

$$\alpha_{mpp} t_{1Nmpp}^2 + \beta_{mpp} t_{1Nmpp} + \gamma_{mpp} = 0, \tag{28}$$

where

$$\alpha_{mpp} = -2\pi V_N (1 + K_1 I_N), \tag{29}$$

$$\beta_{mpp} = -[(2K_2 - 3\pi) V_N + \pi K_1 (2 - V_N) I_N], \tag{30}$$

$$\gamma_{mpp} = (K_2 - \pi) V_N, \tag{31}$$

Only the positive solution for $t_{1Nmpp}$ has a physical meaning:

$$t_{1Nmpp} = \frac{-\beta_{mpp} - \sqrt{\beta_{mpp}^2 - 4\alpha_{mpp}\gamma_{mpp}}}{2\alpha_{mpp}}, \tag{32}$$

Translating the normalized time (32) to the real-time yields:

$$t_{1mpp} = \frac{T}{2} t_{1Nmpp}, \tag{33}$$

The results of (32), and (33) allow for optimally locating the power transfer window for optimal energy harvesting; see (27).

## 3. Comparison with the Experimental Results

An experimental laboratory OLMEH prototype, as shown in Figure 1, and its power processing unit were built and tested. The OLMEH's core was constructed by stacking together three pairs of 10H10 C-cores made of silicon steel (EILOR MAGNETIC CORES). The magnetic path length was $l_c$ = 120 mm, and the total core cross-section of $A_c$ = 1800 mm$^2$. The total number of secondary turns was $N$ = 40.

NTP011N115MC MOSFETs and Schottky rectifiers STP80H100TV were used. The prototype controller was developed and built to allow for adjustment of the delay time, $t_1$, and the controller's power transfer window width, $t_{pw}$, independently.

The Froelich parameters of the core $a$ and $b$ were established by curve fitting to the experimental data. Measured B-H characteristics of a silicon steel core sample vs. the fitted BH curve, drawn by using the extracted Froelich parameters, are shown in Figure 6. Here, $a$ = 2.05 [T] and $b$ = 109.4 [At/m] were found, the same as in [10].

Typical waveforms of the experimental OLMEH with an active rectifier at line current $I_1$ = 100 A rms under constant voltage load, $V_b$ = 45 V, are shown in Figure 7. Here, the waveforms shown are: line current $i_1(t)$, the rectifier input current $i_{in}(t)$, and the gating signal of the M1 switch, $v_g(t)$, generated by the controller. The math channel shows the instantaneous output power $p_o(t)$. Recall that energy transfer to the CVL occurs during the

high level of the $v_1(t)$ waveform. Note that the primary voltage, $v_1(t)$, was measured across the line conductor segment of only about 10 cm long. Also, it is worth noting that (during the positive half cycle), the saturation of the core manifests itself by the rapidly falling edge of the $i_{in}(t)$ current. The energy stored by the magnetizing inductor manifests itself by the offset segment seen in the $i_{in}(t)$ waveform, when the $v_1(t)$ is at its zero level. The release of the stored energy is manifested by the down-going step in the $i_{in}(t)$ waveform.

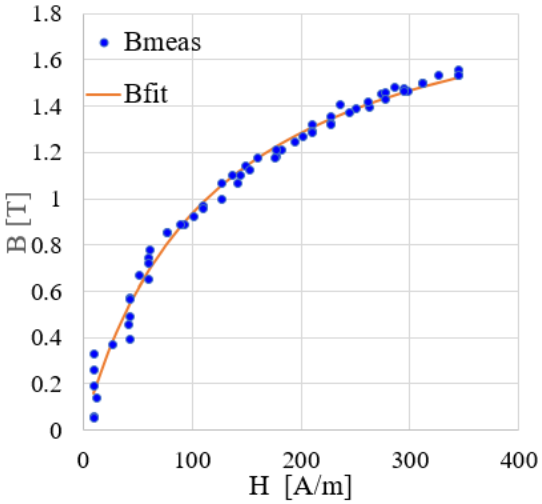



**Figure 6.** Comparison of the measured BH curve of the silicon steel core sample (EILOR MAGNETIC CORES) to its Froelich approximation [10].

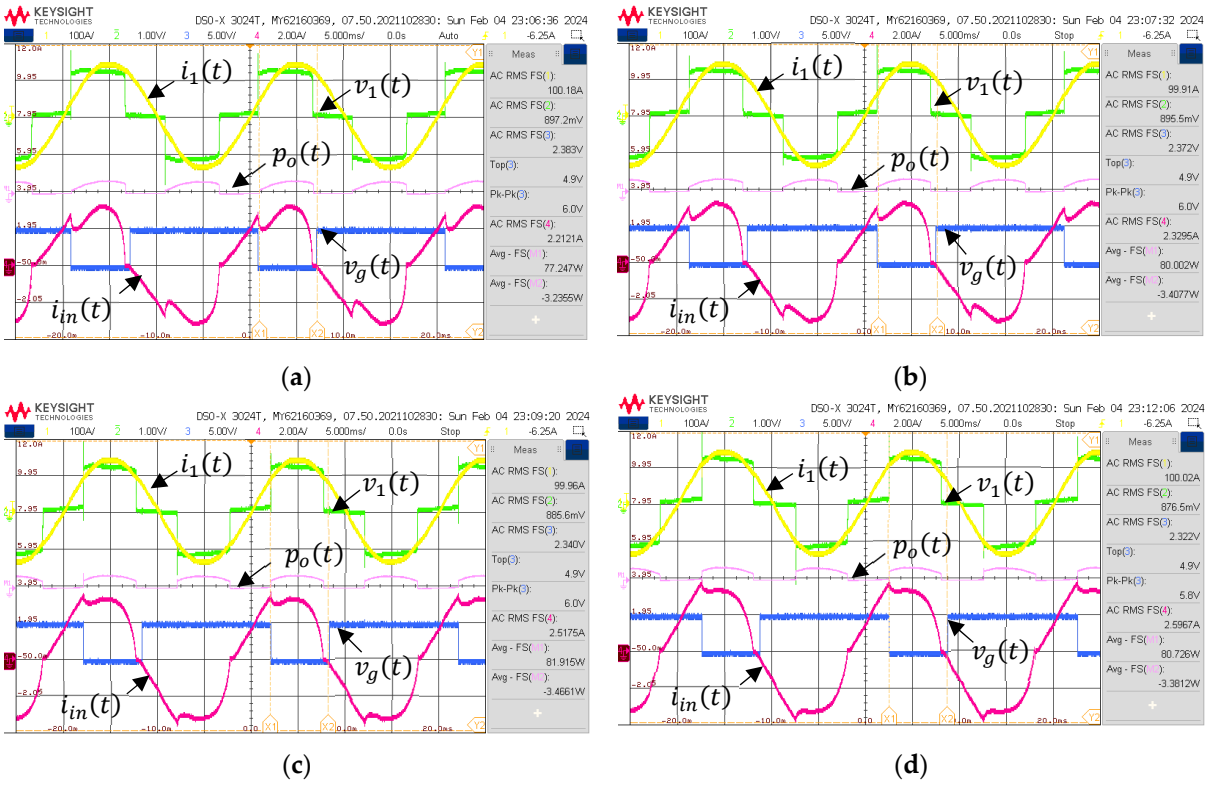



**Figure 7.** *Cont.*

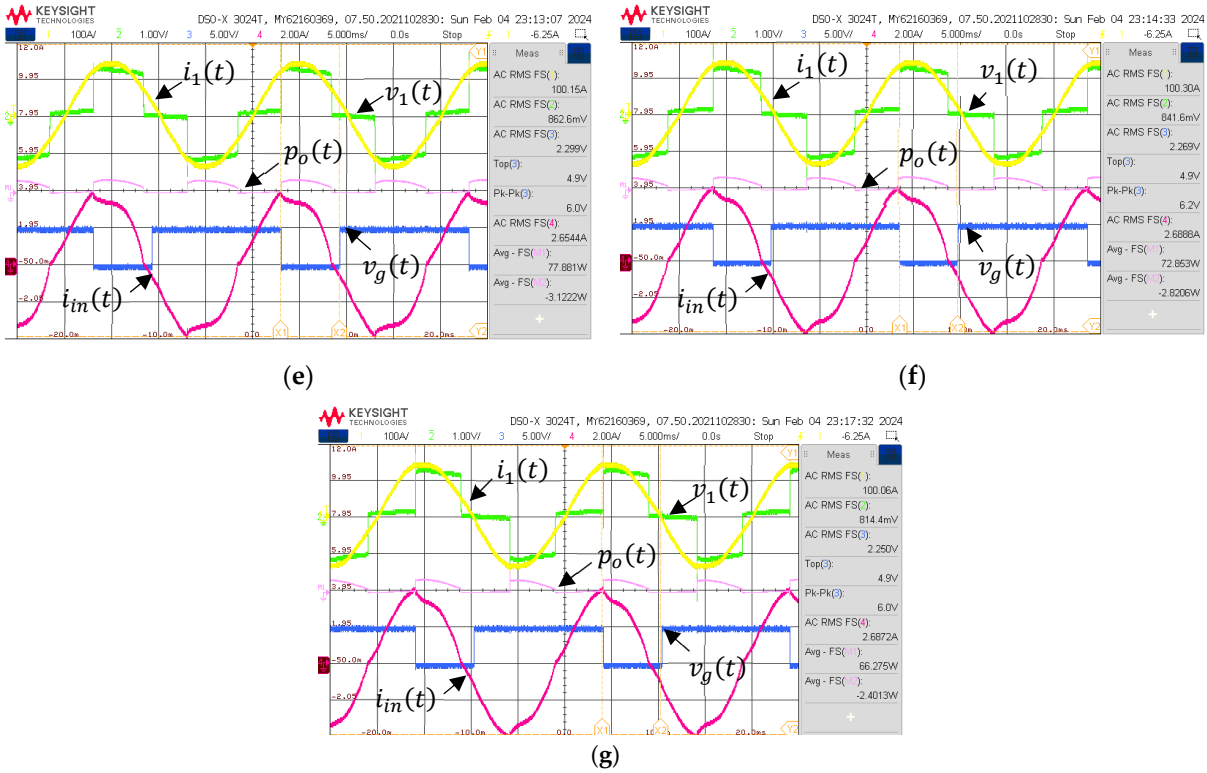



**Figure 7.** Typical waveforms of the experimental OLMEH with an active rectifier at line current $I_1$ = 100 A rms: $V_b$ = 45 V. Delay time: (**a**) $t_1$ = 1 mS; (**b**) $t_1$ = 1.5 mS; (**c**) $t_1$ = 2 mS; (**d**) $t_1$ = 2.5 mS; (**e**) $t_1$ = 3 mS; (**f**) $t_1$ = 3.5 mS; (**g**) $t_1$ = 4 mS.

The theoretical derivations were first verified by simulation. Figure 8 shows the comparison of the calculated vs. the simulated results for the output power. Here, the assumed line current was $I_{line}$ = 100 A rms and $I_{line}$ = 200 A rms (also $N$ = 40, $V_b$ = 45 V). Good agreement between the results was found.

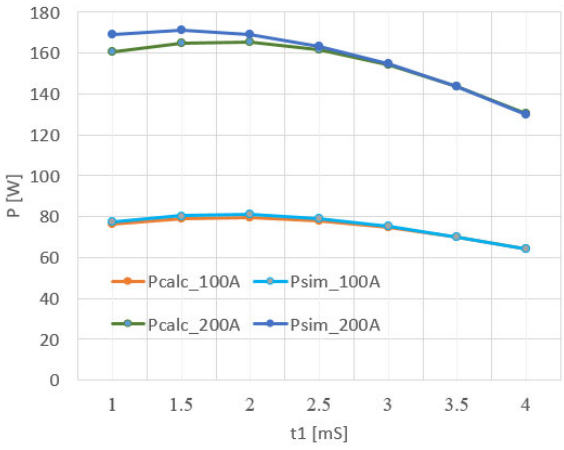



**Figure 8.** Comparison of the simulated vs. calculated OLMEH's output power as a function of the delay time, $t_1$, for line current of $I_{line}$ = 100 A rms and $I_{line}$ = 200 A rms, (here, $N$ = 40 and $V_b$ = 45 V).

Comparison of the experimentally measured vs. calculated by (33) and (27) output power as a function of the delay time $t_1$, for line current $I_{line}$ = 100 A rms and constant load voltage $V_b$ = 45 V, as shown in Figure 9. A good match between the experimental and theoretically predicted power can be observed.

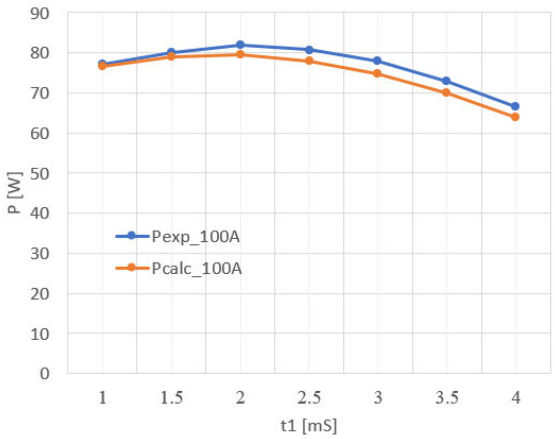
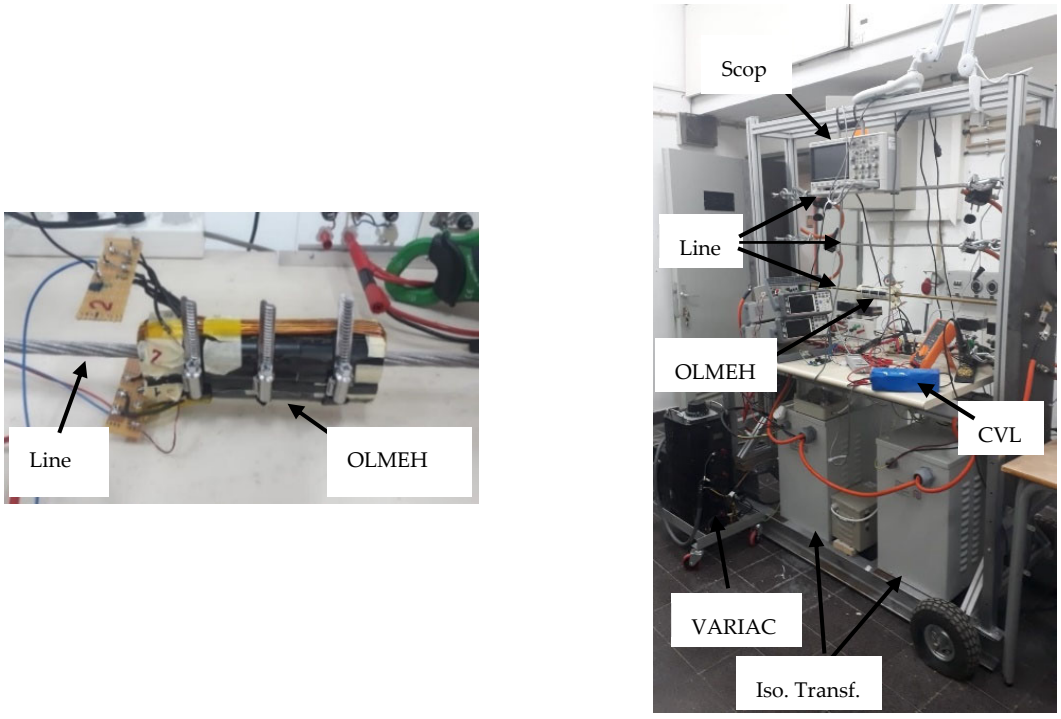



**Figure 9.** Comparison of the experimentally measured vs. calculated output power as a function of the delay time $t_1$. (For $I_{line}$ = 100 A rms; $V_b$ = 45 V).

The experimental work revealed that handling the OLMEH prototype brought about variations in its magnetic properties, primarily due to variations in the technological air gap between the two halves of the C-core, which depend on factors like mounting force and surface imperfections. Therefore, some inaccuracies can be seen in the presented comparison plots.

The view of the experimental prototype OLMEH and its test bench are shown in Figures 10a and 10b, respectively, and they are similar to that used in [10].




(**a**) (**b**)

**Figure 10.** View of the experimental prototype OLMEH (**a**) and its test bench (**b**) [10].

## 4. Conclusions

This paper aims to offer a closed-form solution for an overhead line magnetic energy harvester with an active rectifier (OLMEH-AR) operating under a constant voltage load.

The article initially examines the Froelich equation, which is subsequently utilized as a fundamental instrument to scrutinize the OLMEH-AR's functionality. The selection

of the Froelich equation as the approximation function to characterize the core BH curve is crucial and has been demonstrated to be well suited for facilitating the derivation of a comprehensive analytical model of an OLMEH-AR. The offered model allowed for an extensive analytical study of the OLMEH-AR which yielded approximate analytical solutions for charging and idle periods, the power transfer window, the mean output current, and the mean output power.

An important note drawn from the experimental work is that manipulating the OLMEH-AR prototype affects the magnetic core parameters. This is primarily due to variations in the technological air gap remaining between the two halves of the C-core, which depend on factors such as misalignment, mounting force, and surface imperfections. Therefore, the authors believe that developing a more precise and complex theoretical model, including hysteresis effects, temperature effects, etc., is of limited practical value because of the unavoidable core parameter variations.

As compared to the passive rectifier case, the application of an active rectifier significantly increases the harvester's output power [10]. This comes as a result of two key features, which the passive rectifier does not possess. First is that the controlled rectifier allows for the storage of magnetic energy by short-circuiting the OLMEH's secondary winding, and, secondly, the active rectifier allows aligning the power transfer window to track the optimal power point. The output characteristics of the OLMEH and its proper matching, considering variable line current and load voltage conditions, have also been reported in recent papers [23–25].

While the advantage of the uncontrolled rectifier is its simplicity and robustness, the advantages of the active rectifier are the ability to control the CVL charging current as well as providing overcharge and line overcurrent protection features. However, realizing the active rectifier functions requires a somewhat sophisticated approach, synchronized to the line current control circuit.

**Author Contributions:** Conceptualization, A.K.; methodology, A.A.; software, A.A.; validation, A.A. and M.S.; formal analysis, A.A.; investigation, A.A.; resources, A.K.; data curation, M.S.; writing—original draft preparation, A.A.; writing—review and editing, A.A.; visualization, A.A. and M.S.; supervision, A.K.; project administration, A.K.; funding acquisition, A.K. All authors have read and agreed to the published version of the manuscript.

**Funding:** This research received no external funding.

**Institutional Review Board Statement:** Not applicable.

**Informed Consent Statement:** Not applicable.

**Data Availability Statement:** The original contributions presented in the study are included in the articl, further inquiries can be directed to the corresponding author.

**Conflicts of Interest:** The authors declare no conflicts of interest.

## Nomenclature

Throughout this paper, the following definitions of key parameters were adopted.

| | |
|---|---|
| Time (continuous) | $t$ |
| State 1 termination instant | $t_1$ |
| State 2 termination instant | $t_2$ |
| Flux density zero crossing instant | $t_Z$ |
| Power line angular frequency | $\omega$ |
| Flux density | $B(t)$ |
| Saturation flux density | $B_s$ |
| Field intensity | $H(t)$ |
| Saturation field intensity | $H_s$ |
| Froelich coefficients | $a, b$ |
| Number of turns | $N$ |
| Magnetic path length | $l_c$ |

| | |
|---|---|
| Magnetic core area | $A_c$ |
| Line (primary) current instantaneous | $i_1(t)$ |
| Line (primary) current amplitude | $I_{1m}$ |
| Secondary current instantaneous | $i_2(t)$ |
| Secondary current amplitude | $I_{2m}$ |
| Magnetizing current, (instantaneous) | $i_m(t)$ |
| Rectifiers' input (AC side) voltage | $v_{in}(t)$ |
| Rectifiers' input (AC side) current | $i_{in}(t)$ |
| CVL voltage | $V_b$ |
| CVL current | $i_b(t)$ |
| Average output power | $P_o$ |

## Appendix A

In our case, the delay angle is $\theta = \omega t_1$ and the extinction angle is $\vartheta + \delta = \omega t_2$. We found the condition on $\vartheta$ maximizing the function $\cos(\vartheta) - \cos(\vartheta + \delta)$.

Applying the classical extremum finding procedure:

$$\frac{d}{d\vartheta}(\cos(\vartheta) - \cos(\vartheta + \delta)) = -\sin(\theta) + \sin(\vartheta + \delta) = -\sin\vartheta + \sin\vartheta\cos\delta + \cos\vartheta\sin\delta = 0 \quad \text{(A1)}$$

whence

$$\tan\vartheta = \frac{\sin\delta}{1 - \cos\delta} = \frac{2\sin\frac{\delta}{2}\cos\frac{\delta}{2}}{2\left(\sin\frac{\delta}{2}\right)^2} = \cot\frac{\delta}{2} = \tan\left(\frac{\pi}{2} - \frac{\delta}{2}\right), \quad \text{(A2)}$$

Comparison of the argument on the left hand-side and the right hand-side yields the delay angle:

$$\vartheta = \frac{\pi}{2} - \frac{\delta}{2}, \quad \text{(A3)}$$

whence the extinction angle is

$$\vartheta + \delta = \frac{\pi}{2} + \frac{\delta}{2}. \quad \text{(A4)}$$

Hence, to attain the MPP condition, the pulse edges should be aligned symmetrically relative to $\pi/2$; thus, (26) follows.

## References


1. Kang, S.; Yang, S.; Kim, H. Non-intrusive voltage measurement of ac power lines for smart grid system based on electric field energy harvesting. *Electron. Lett.* **2017**, *53*, 181–183. [CrossRef]
2. Moghe, R.; Lambert, F.C.; Divan, D. Smart "stick-on" sensors for the smart grid. *IEEE Trans. Smart Grid* **2012**, *3*, 241–252. [CrossRef]
3. Moghe, R.; Iyer, A.R.; Lambert, F.C.; Divan, D.M. A low-cost wireless voltage sensor for monitoring MV/HV utility assets. *IEEE Trans. Smart Grid* **2014**, *5*, 2002–2009. [CrossRef]
4. Gu, I.Y.H.; Sistiaga, U.; Berlijn, S.M.; Fahlstrom, A. Online detection of snow coverage and swing angles of electrical insulators on power transmission lines using videos. In Proceedings of the 16th IEEE International Conference on Image Processing (ICIP 2009), Cairo, Egypt, 7–10 November 2009; pp. 3249–3252. [CrossRef]
5. Zhong, Y.-P.; Zuo, Q.; Zhou, Y.; Zhang, C. A new image-based algorithm for icing detection and icing thickness estimation for transmission lines. In Proceedings of the IEEE International Conference on Multimedia and Expo Workshops (ICMEW), San Jose, CA, USA, 15–19 July 2013; pp. 1–6. [CrossRef]
6. Riba, J.-R.; Moreno-Eguilaz, M.; Bogarra, S. Energy Harvesting Methods for Transmission Lines: A Comprehensive Review. *Appl. Sci.* **2022**, *12*, 10699. [CrossRef]
7. Moon, J.; Leeb, S.B. Power Electronic Circuits for Magnetic Energy Harvesters. *IEEE Trans. Power Electron.* **2016**, *31*, 270–279. [CrossRef]
8. Enayati, J.; Asef, P. Review and Analysis of Magnetic Energy Harvesters: A Case Study for Vehicular Applications. *IEEE Access* **2022**, *10*, 79444–79457. [CrossRef]
9. Deng, Z.; Dapino, M.J. Review of magnetostrictive vibration energy harvesters. *Smart Mater. Struct.* **2017**, *26*, 103001. [CrossRef]
10. Abramovitz, A.; Shwartsas, M.; Kuperman, A. Nonlinear Analysis and Closed-Form Solution for Overhead Line Magnetic Energy Harvester Behavior. *Appl. Sci.* **2024**, *14*, 9146. [CrossRef]
11. Moon, J.; Leeb, S.B. Wireless sensors for electromechanical system diagnostics. *IEEE Trans. Instr. Meas.* **2018**, *67*, 2235–2246. [CrossRef]

12. Liu, Z.; Li, Y.; Duan, N.; He, Z. An energy management method for magnetic field energy harvesters under wide-range current in railway electrification systems. *IEEE Trans. Ind. Electron.* **2024**, *71*, 5360–5369. [CrossRef]
13. Monagle, D.; Ponce, E.A.; Leeb, S.B. Rule the Joule: An energy management design guide for self-powered sensors. *IEEE Sens. J.* **2024**, *24*, 6–15. [CrossRef]
14. Suntio, T.; Viinamaki, J.; Jokipii, J.; Messo, T.; Kuperman, A. Dynamic characterization of power electronic interfaces. *IEEE J. Emerg. Sel. Top. Power Electron.* **2014**, *2*, 949–961. [CrossRef]
15. Monagle, D.; Ponce, E.; Leeb, S.B. Generalized analysis method for magnetic energy harvesters. *IEEE Trans. Power Electron.* **2022**, *37*, 15764–15773. [CrossRef]
16. Li, Y.; Duan, N.; Liu, Z.; Hu, J.; He, Z. Impedance-matching-based maximum power tracking for magnetic field energy harvesters using active rectifiers. *IEEE Trans. Ind. Electron.* **2023**, *70*, 10730–10739. [CrossRef]
17. Chen, F.; Yang, C.; Guo, Z.; Wang, Y.; Ma, X. A magnetically controlled current transformer for stable energy harvesting. *IEEE Trans. Power Deliv.* **2023**, *38*, 212–221. [CrossRef]
18. Kuperman, A.; Averbukh, M.; Lineykin, S. Maximum power point matching versus maximum power point tracking for solar generators. *Renew. Sustain. Energy Rev.* **2013**, *19*, 11–17. [CrossRef]
19. Moon, J.; Leeb, S.B. Analysis Model for Magnetic Energy Harvesters. *IEEE Trans. Power Electron.* **2015**, *30*, 4302–4311. [CrossRef]
20. Gao, M.; Yi, L.; Moon, J. Mathematical modeling and validation of saturating and clampable cascaded magnetics for magnetic energy harvesting. *IEEE Trans. Power Electron.* **2023**, *38*, 3455–3468. [CrossRef]
21. Vos, M.J. A magnetic core permeance model for inductive power harvesting. *IEEE Trans. Power Electron.* **2020**, *35*, 3627–3635. [CrossRef]
22. Liu, Z.; Li, Y.; Yang, H.; Duan, N.; He, Z. An accurate model of magnetic energy harvester in the saturated region for harvesting maximum power: Analysis, design and experimental verification. *IEEE Trans. Ind. Electron.* **2023**, *70*, 276–285. [CrossRef]
23. Abramovitz, A.; Shvartsas, M.; Orfanoudakis, G.I.; Kuperman, A. Output Characteristics of Passive Magnetic Energy Harvester Feeding a Constant-Voltage-Type Load. *IEEE J. Emerg. Sel. Top. Power Electron.* **2024**, *in press*. [CrossRef]
24. Abramovitz, A.; Shvartsas, M.; Kuperman, A. Enhanced Maximum Power Point Reaching Method for Passive Magnetic Energy Harvesters Operating Under Low Primary Currents. *IEEE Trans. Power Electron.* **2024**, *39*, 6619–6623. [CrossRef]
25. Abramovitz, A.; Shvartsas, M.; Kuperman, A. On the Maximum Power of Passive Magnetic Energy Harvesters Feeding Constant Voltage Loads Under High Primary Currents. *IEEE Trans. Power Electron.* **2024**, *39*, 12076–12080. [CrossRef]


**Disclaimer/Publisher's Note:** The statements, opinions and data contained in all publications are solely those of the individual author(s) and contributor(s) and not of MDPI and/or the editor(s). MDPI and/or the editor(s) disclaim responsibility for any injury to people or property resulting from any ideas, methods, instructions or products referred to in the content.